

A photospheric and chromospheric activity analysis of the quiescent retrograde-planet host ν Octantis A

D. J. Ramm^{1*}†, P. Robertson², S. Reffert³, F. Gunn¹, T. Trifonov⁴, K. Pollard¹,
F. Cantalloube⁴

¹ School of Physical and Chemical Sciences, University of Canterbury, Private Bag 4800, Christchurch 8140, New Zealand

² Department of Physics & Astronomy, The University of California, Irvine, Irvine, CA 92697, USA

³ Landessternwarte, Zentrum für Astronomie der Universität Heidelberg, Königstuhl 12, 69117, Heidelberg, Germany

⁴ Max-Planck-Institut für Astronomie, Königstuhl 17, Heidelberg 69117, Germany

27 December 2021

ABSTRACT

The single-lined spectroscopic binary ν Octantis provided evidence of the first conjectured circumstellar planet demanding an orbit retrograde to the stellar orbits. The planet-like behaviour is now based on 1437 radial velocities (RVs) acquired from 2001 to 2013. ν Oct’s semimajor axis is only 2.6 au with the candidate planet orbiting ν Oct A about midway between. These details seriously challenge our understanding of planet formation and our decisive modelling of orbit reconfiguration and stability scenarios. However, all non-planetary explanations are also inconsistent with numerous qualitative and quantitative tests including previous spectroscopic studies of bisectors and line-depth ratios, photometry from *Hipparcos* and the more recent space missions *TESS* and *Gaia* (whose increased parallax classifies ν Oct A closer still to a subgiant, \sim K1 IV). We conducted the first large survey of ν Oct A’s chromosphere: 198 Ca II H-line and 1160 H α indices using spectra from a previous RV campaign (2009–2013). We also acquired 135 spectra (2018–2020) primarily used for additional line-depth ratios, which are extremely sensitive to the photosphere’s temperature. We found no significant RV-correlated variability. Our line-depth ratios indicate temperature variations of only ± 4 K, as achieved previously. Our atypical Ca II analysis models the indices in terms of S/N and includes covariance significantly in their errors. The H α indices have a quasi-periodic variability which we demonstrate is due to telluric lines. Our new evidence provides further multiple arguments realistically only in favor of the planet.

Key words: methods: data analysis – stars: activity – binaries: spectroscopic – planetary systems – individual: ν Octantis – planet-star interactions

1 INTRODUCTION

A decade or so after the first exoplanets were described (Wolszczan & Frail 1992; Mayor & Queloz 1995), radial velocity (RV) evidence for the first retrograde planet appeared from a very unexpected source, the compact single-lined spectroscopic binary ν Octantis (Ramm 2004). However, these RVs shared the same initial fate as those from γ Cep A which almost hosted the first acknowledged RV-discovered planet (Campbell, Walker & Young 1988; Walker et al. 1992). γ Cep Ab was eventually confirmed 15 yr later (Hatzes et al. 2003), and was then the shortest period binary with a planet ($P_{\text{bin}} \sim 57$ yr) – about $20\times$ longer than that for ν Oct. Both initial series of RVs led their discoverers to describe both planet and stellar rotation-related scenarios, the latter then being suspected as

more likely causes. These two binaries have many other parallel details in their exoplanet histories and host star characteristics.¹

Host stars may provide evidence that a candidate exoplanet orbit is retrograde relative to the star’s rotation (which we label type-1), and if in a binary system, relative to the two stellar orbits (our type-2). The first acknowledged retrograde planet was HAT-P-7b, promptly identified using the McLaughlin-Rossiter effect (our type-1; Winn et al. 2009; Narita et al. 2009). This had been preceded in the same year by the first paper describing the conjectured planet ν Oct Ab, (Ramm et al. 2009; henceforth R09), which has proven to be much more challenging for establishing its reality beyond reasonable doubt. This is almost entirely due to the unprece-

¹ For example, and very significantly, both hosts were originally classified as giants, rare for early exoplanet claims – and both K0 III – which made a stellar origin for the RV signals more tenable. They also share a trivial near-polar declination detail: $|\delta| = 77^\circ$.

* E-mail: djr1817@gmail.com

† Research Fellow

dented geometry of the conjectured system, whose stars are separated by only 2–3 au with the circumstellar i.e. S-type planet about midway between (see e.g. Gong & Ji 2018; Bonavita & Desidera 2020; Quarles et al. 2020). Some details for ν Oct (HD 205478, HIP 107089) and its conjectured planet (based on the persistent RV cycle with a period $P_{RV} \sim 415$ d) are listed in Table 1 and Table 2. The parallax was recently updated from *Gaia* observations, and critically for the planet claim, increased by about 10 per cent (Gaia Collaboration 2018; Kervella et al. 2019 - whose work specifically includes nearby stars with stellar and substellar companions).²

The system’s geometry makes a prograde planet impossible (R09; Eberle & Cuntz 2010). An S2 (i.e. S-type, our type-2 retrograde) orbit has a significantly wider stability zone than its prograde equivalent (see e.g. Jefferys 1974; Wiegert & Holman 1997; Morais & Giuppone 2012).³ This opportunity for ν Oct Ab’s reality was first investigated by Eberle & Cuntz (2010), and subsequently by Quarles, Cuntz & Musielak (2012), Goździewski et al. (2013) and Ramm et al. (2016; henceforth R16), all of which found retrograde solutions with merit but without being conclusive. Meanwhile, however, multiple other tests demonstrate that all other explanations (e.g. measurement artefacts, stellar variability, ν Oct being a triple-star system) are substantially less credible than the planet (R09; Ramm 2015 - henceforth R15; and R16). If the planet is an illusion, ν Oct A so far provides no evidence of its causative role other than the persistent precise cycle of so far 1437 RVs over 12.5 yr, and thus would have the alternative distinction of seriously confronting our understanding of stellar variability.⁴

Goździewski et al. identify a small number of nearby mean motion resonances for coplanar S2 orbits in ν Oct including one at the period ratio 5:2, this having been qualitatively suspected in R09. The unprecedented strong interactions suggest resonance is likely to be a contributing factor for stability, as in other multi-body systems (e.g. Campanella 2011; Robertson et al. 2012; Horner et al. 2019; Stock et al. 2020). ν Oct Ab would never be confined to a typical narrow orbital path but would move endlessly throughout a rather wide zone as Eberle & Cuntz (2010) first illustrated, leading to significant challenges for competing models trying to characterize different orbital geometries (Panichi et al. 2017).

Many S-type planets have now been reported, though demands for any following an S2 orbit remains rare since the binary must be quite compact to lead to this conclusion. Scenarios that may create such orbits include star-hopping (Kratter & Perets 2012), perhaps facilitated by a scattering event, or significant system or orbital changes involving stellar winds, accretion/debris discs or evolution to a white dwarf (WD) companion (see e.g. Tutukov & Ferorova 2012). The WD scenario may have support for ν Oct from spec-

Parameter	ν Octantis A	Reference
Spectral type ^a	K1IIIb-IV	(1)
V (mag)	$+3.738 \pm 0.005$	(2)
parallax (mas)	51.546 ± 0.705	(3)
M_V (mag)	$+2.30 \pm 0.16$	our calculation
BC_V (mag)	-0.39 ± 0.05	(2)
H_p (<i>Hipparcos</i> mag)	3.8981 ± 0.0004	(4)
Mass (\mathcal{M}_\odot) ^a	$1.61 \pm 0.15, 1.4 \pm 0.3$	(2), (5)
Radius (\mathcal{R}_\odot) ^a	$5.81 \pm 0.12, 6.0 \pm 0.3$	(2), (5)
T_{eff} (K) ^a	$4860 \pm 40, 4815 \pm 90$	(2), (5)
T_{LDR} (K) ^b	$4811 \pm 45, 4810 \pm 45$	(1), (6)
Luminosity (\mathcal{L}_\odot) ^a	~ 17	(5)
$v \sin i$ (km s ⁻¹)	2 ± 0.5	(2)
P_{rot} (d) ^a	$\simeq 140 \pm 35$	(6)
Age (Gyr)	$\sim 2.5\text{--}3$	(5)
Observations (RVs) ^c	1180 I ₂ -cell, 257 CCF	(1), (5)
time span of RVs	2001.43 – 2013.96	(1), (5)

Table 1. Stellar parameters and RV observations for ν Oct A (all errors are $\pm 1\sigma$, except H_p which is the standard error on the median). 1: Ramm et al. (2016), 2: Fuhrmann & Chini (2012), 3: Kervella et al. (2019): this parallax is a Bayesian ZP-corrected value from ESA’s *Gaia* mission (GRD2: Gaia Collaboration 2018), 4: ESA (1997), 5: Ramm et al. (2009), 6: Ramm (2015). ^a Reviewed in § 3.5. ^b LDR: line-depth ratio analysis. ^c See Footnote 4.

Parameter	Binary	planet, Ab
Companion Mass	$0.5 - 0.6 \mathcal{M}_\odot$	$2.1 - 2.6 \mathcal{M}_{\text{Jup}}$
Object class	K7 – M0V, or WD	Jovian
K	7.05 km s^{-1}	$40 - 45 \text{ m s}^{-1}$
a (au)	$2.5 - 2.6$	$1.2 - 1.3$
P_{orb}	$1050.1 \text{ d} \simeq 2.9 \text{ yr}$	$415 - 418 \text{ d}$
e	0.24	$0.09 - 0.13$

Table 2. Basic orbital parameters for ν Oct and the conjectured S2-type retrograde planet, summarised from R09, Goździewski et al. (2013) and R16. The ratio of the orbital periods, P_{orb} , is close to 5:2. Quarles et al. (2012) and Goździewski et al. (2013) both favour a coplanar planetary orbit which R16 could not confirm.

trophotometric observations nearly 50 yr ago (Arkharov, Hagen-Thorn & Ruban 2005). They reported unusually large variability ($S_\nu = 0.14$ mag) in the near ultraviolet (345 nm) in the 1970s. Of the 172 ‘normal’ and 176 ‘suspect variable’ stars they catalogued, only two others had larger S_ν , both in the latter group. This may be a clue to the nature of ν Oct B as it seems unlikely ν Oct A is the source.

The first close-planet candidate for a WD host was recently reported (WD1856+534; Vanderburg et al. 2020), discovered using NASA’s Transiting Exoplanet Survey Satellite (TESS; Ricker et al. 2015), another space mission that should help unravel the ν Oct mystery. WD1856 b’s orbit ($P_{\text{pl}} \sim 1.4$ d), is presumed to be due to reconfiguration and migration processes (see e.g. Lin, Bodenheimer & Richardson 1996; Rasio & Ford 1996), which must have relevance for any orbitally retrograde planet. Together with mass loss/transfer processes inherent in WD evolution, these scenarios may further complicate attempts to understand ν Oct Ab but also provide some advantage since orbit reconfiguration (of the planet or the binary) would not require interaction from external or other internal masses, as anticipated with an unevolved secondary star.

Two other recent claims are also relevant here. Firstly, another

² Thus ν Oct A is less luminous and should be classified closer still to a subgiant, \sim K1 IV, as now is also γ Cep A (Hatzes et al. 2003; Fuhrmann 2004). § 3.5 will discuss this important revision.

³ With zero evidence for retrograde status we label the orbit type-0 i.e. prograde, and assumed if not stated. If the host provides evidence of both type-1 and 2 we would label it type-3 (1+2). The scheme is applicable to single star hosts i.e. type 0 or 1, and both S- (circumstellar) and P-type (circumbinary) planets (Dvorak 1986), i.e. type 0, 1, 2 or 3.

⁴ The RVs were obtained using two CCDs and different calibration techniques (I₂-cell and thorium-argon spectra) and therefore also different reduction methods. No other star’s study using our instruments and methods provide any similar planet-like RVs. The primary star’s argument of periastron, $\omega_1 = 75^\circ$, has not changed significantly in 95 yr so any claim that a hierarchical triple-star system is creating the planet-like RVs is also unfounded (see R09 and R16 for details).

S2-type planet, HD 59686 Ab, has been conjectured in this somewhat wider but rather eccentric binary (Ortiz et al. 2016; Trifonov et al. 2018; K2 III, $a_{\text{bin}} \sim 13.6$ au, $e_{\text{bin}} \sim 0.7$). Interestingly, HD 59686 B is also suspected of being a WD, leading Ortiz et al. to investigate one possibility that the planet formed from a second generation protoplanetary disc. It is tempting to speculate that ν Oct and HD 59686 may be two early examples of relatively compact binaries with WD secondaries that created S2-type planets. Secondly, the first planet in a binary more compact than ν Oct was recently reported (HD 42936, K0V + L dwarf; $a_{\text{bin}} \sim 1.2$ au; Barnes et al. 2020). HD 42936-Ab is close to its host (~ 0.066 au) so both it and WD1856 b are assumed to have reconfigured orbits, but with no evidence demanding either be retrograde.

Understandable suspicion also persists that ν Oct A’s RV signal may be due to undetected surface activity. Hatzes et al. (2018) repeated this concern after γ Dra’s anticipated single-planet claim disappeared after more RV data was acquired. Oscillatory convective modes (Saio et al. 2015) were instead promoted as the variable RVs more likely origin, just as Reichert et al. (2019) speculate for Aldebaran – instead of its conjectured planet (Hatzes et al. 2015). But unlike ν Oct A which is a relatively unevolved low-luminosity star (and so far has a persistent periodic RV signal), γ Dra ($\sim 500 L_{\odot}$, $50 R_{\odot}$), and Aldebaran ($\sim 400 L_{\odot}$, $40 R_{\odot}$) typify the theoretical high-luminosity expectations of a star having these convective modes. Both are classified K5 III and are reminders of the potential complications such evolved stars, both real and mistaken (e.g. ν Oct A and γ Cep A) can present. Other radial and non-radial oscillations in stars similar to ν Oct A instead have a complex power spectrum that complicate asteroseismology studies (see e.g. Dupret et al. 2009). This is not at all consistent with the planet-like RV signal ν Oct A has provided to date. Hence, if ν Oct A is deceiving us, a more reasonable concern is that stars more similar to it are more likely to be creating well-crafted illusions, such as γ Cep A. This possibility would create significant complications for other exoplanet claims now and in the future, and perhaps not restricted to similar subgiants.

This background has motivated the photospheric and chromospheric studies reported here. Photospheric line variations are critical for RVs but also for the extremely temperature-sensitive method of line-depth ratios (LDRs; e.g. Hatzes, Cochran & Bakker 1998; Gray & Brown 2001; Kovtyukh et al. 2003; R15; R16). R15 and R16 demonstrate temperature constancy for ν Oct A to as little as ± 4 K over 12 yr, with high consistency with the very low photometric variability recorded by *Hipparcos* (see Table 1). This latest LDR series is also relevant as, more or less concurrently, observations have also been obtained by NASA’s TESS mission which significantly support ν Oct A’s photometric stability, as well as RVs from ESO’s HARPS spectrograph (Trifonov et al., in preparation).

Chromosphere activity of ν Oct A has so far been limited to three eye estimates of the Ca II K line from each of two spectra (Warner 1969), a single spectrum of Ca II H & K (R09) and H-line indices from 17 spectra (R16). All three papers concluded ν Oct A had minimal Ca II activity. Additionally, the Mg $h + k$ chromospheric emission-line study by Pérez Martínez, Schröder & Cuntz (2011) found ν Oct A’s activity to be very near their sample’s empirically-derived basal flux of 177 cool giants. Here we report on two much larger series: 198 line indices from the Ca II H line and 1160 H α indices.

Our work allows ν Oct A to be characterized in further detail, providing new evidence for the planet since significant activity is again refuted. Even if the planet is eventually proven to be an illusion, which seems to be increasingly unlikely, our work adds to the

fundamental knowledge of the star at the centre of this persistently challenging system.

2 INSTRUMENTATION AND OBSERVATIONS

The data analysed here were acquired in two series, one about a decade ago and the other over the past two years. Both series were obtained at the University of Canterbury Mount John Observatory using the 1-m McLellan telescope and HERCULES, a fibre-fed, thermally insulated, vacuum-housed spectrograph (Hearnshaw et al. 2002). The CCD was a $4k \times 4k$ detector cooled to $\sim -95^{\circ}\text{C}$ which recorded the ν Oct A spectra with a resolving power $R \sim 70\,000$. Further instrument details and our reduction methods for obtaining flat-fielded normalized spectra can be found in Ramm (2004), where the first tentative mention of the conjectured planet is made, and R16. Our reduction software (HRSP; see Skuljan 2004) automatically provides both vacuum and air wavelengths. To make other vacuum-to-air conversions we used the formulae of Morton (2000).

The older series comprises nearly 1200 spectra obtained from 2009.96–2013.96, i.e. four years, and allowed our chromosphere studies of the Ca II H line and H α . The spectra were almost all obtained using an iodine cell that reconfirmed the precise-RV planet-like signal (see R16). For our H α study, 1160 spectra were included in the final analysis, made possible by the higher S/N at these longer wavelengths. The initial sample size for our Ca II analysis was limited to 700 spectra as the Ca II lines were not included in the first year or so of observations. More details of these data sets will follow in the relevant sections.

A smaller set of 135 spectra were acquired more recently, from 2018.34 until 2020.42 i.e. over about 25 months. As the I₂ cell was not used for these observations, we could not obtain further high-precision RVs but instead could use these spectra to obtain a new series primarily of line-depth ratios. The last spectrum obtained (2020.42; JD245 9002) has the highest S/N of our entire series and was acquired to also extend that range of our Ca II spectra. The time span of all spectra considered here is from the first LDR spectrum, 2001.85, until this last observation i.e. ~ 19 yr.

3 PHOTOSPHERE LINE-DEPTH RATIOS

We first present the results from our line-depth-ratio analysis of the new spectra (2018–2020) and compare them to the previously published LDR results (2001–20013 ; R15 and R16) as well as again, the *Hipparcos* photometry (1990–1993). The LDRs demonstrate the continued thermal stability of ν Oct A’s photosphere and so are a useful prelude to our chromosphere studies.

3.1 Old and new LDRs and corresponding temperatures

We used the same methods and pipelines employed in R15 and R16: specifically, for each of the 135 new ν Oct A spectra we constructed 22 LDRs and their errors from ten spectral lines in the wavelength region 6232–6257 Å. The principal equations for these calculations are given in R15.

One significant advantage of LDRs is that they can be used to derive a star’s temperature – which brings additional benefits – using a series of calibration stars whose temperatures allow precise interpolation (see R15; their fig. 1). Further increases in accuracy and precision are achieved by modelling the influences of

temperature and luminosity (i.e. evolution) using linear regression (Press et al. 1994; algorithm *fitexy*) leading to a modified LDR labelled MLDR (see e.g. Gray & Brown 2001; Catalano et al. 2002; R15). R15 reported an accuracy of 45 ± 25 K for recovering the 20 calibration stars’ temperatures but a precision as small as ± 4 K for their 215 ν Oct A LDRs, in excellent agreement with Gray & Brown (2001): their temperature precision from 92 giant stars was 3.9 K. Neglecting these influences can yield significantly poorer temperature statistics as Gray & Brown discuss in the context of other studies.

R15 summarizes the strong relationship between the $T - \text{LDR}$ regression line’s slope s_{reg} and the ratio’s error ϵ_r (see their sec. 4.1). The slope is an indicator of sensitivity of each ratio to the calibration stars’ temperatures. It therefore provides the error on each ratio’s temperature estimate i.e. $\epsilon_{T_r} = s_{\text{reg}} \times \epsilon_r$. Fig. 1 (a) shows the error on each LDR eventually rises exponentially as the spectrum’s S/N drops, as anticipated. We estimated the S/N solely from the photon noise so that $S/N \sim \sqrt{F_c}$ where F_c is the continuum flux at the spectral line, and calculated each ratio’s S/N from the average of the two lines. Our two examples show typical similarities and differences (the relationship illustrated here for the first time), and how ϵ_{T_r} can vary between ratios even though all the lines are within about 25 \AA ($\sim 6232 - 6257 \text{ \AA}$).

The 22 T_{MLDR} values next allow the mean and standard deviation, σ , for each spectrum to be derived, weighted by $w_r = 1/\epsilon_{T_r}^2$. Our average temperatures have no adjustment for any zero-point differences of the T_{MLDR} values for the 22 ratios. The mean values, $\langle T_{\text{MLDR}} \rangle$, and their standard errors ($S.E. = \sigma/\sqrt{22}$) are illustrated in Fig. 1 (b) and (c) respectively. The final standard deviations have an average 30 ± 3 K which is consistent with the temperature accuracy stated above.

The total set of 398 T_{MLDR} values comprises 217 spectra from the first observing series (2001.85–2007.16, 84 nights; R15 and R16), 46 spectra acquired during the I_2 -RV campaign but without the I_2 cell (2011.22–2013.74, 20 nights; R16), and our data (26 nights). The distribution of all of these LDRs in terms of S/N is provided in Fig. 1 (b). This shows that T_{MLDR} becomes less scattered as S/N increases, particularly for $S/N \gtrsim 250$, though this may just be an artefact of the smaller sample size. It can also be seen that all of the spectra with $S/N \lesssim 120$ were obtained in our latest series.

3.2 Final temperature statistics and periodogram

The more recent 135 spectra give a weighted mean temperature $T_{\nu\text{Oct}} = 4810 \pm 4$ K, with no significant difference from the values reported in R15 and R16. Our errors yield $\chi_\nu^2 \sim 0.7$ which indicates their average (~ 6 K) is somewhat more than what would be consistent with our tiny temperature variations. The three series combined have a weighted mean $T_{\nu\text{Oct}} = 4811 \pm 4$ K. If the temperature-recovery accuracy given above (45 ± 25 K) is added in quadrature to this, the final temperature estimate for the 2018–2020 spectra is 4810 ± 45 K, equalling the other two LDR temperatures in Table 1 – Ref. (1) and (6).

Fig. 2 illustrates the distributions of the mean T_{MLDR} values for the 130 epochs of the LDR spectra acquired over 18.6 yr. The means are weighted by the standard errors $w = 1/\epsilon_{T_\star}^2$ where we abbreviate T_{MLDR} with T_\star . Our results display an extraordinary degree of relative accuracy between the three T_{MLDR} series – the offset of the three mean temperatures is remarkably tiny at about 1 K (see $T_{\nu\text{Oct}}$ values in Fig. 2). So whilst the absolute accuracy of

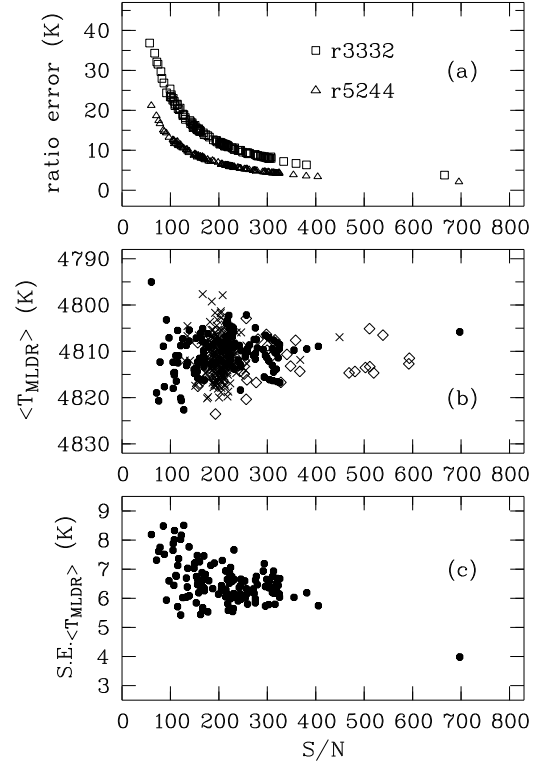


Figure 1. Temperatures (T_{MLDR}) and errors from modified line-depth ratios in terms of S/N . (a) Temperature-calibrated errors, ϵ_{T_r} , for two ratios; e.g. ‘3332’ labels the line pair 6233 \AA and 6232 \AA . (b) Averaged T_{MLDR} values for 398 spectra: ‘x’ 217 LDRs (2001–2007), ‘◇’ 46 LDRs (2011–2013), ‘●’ 135 LDRs (2018–2020). (c) Standard errors on $\langle T_{\text{MLDR}} \rangle$. (a) and (c) include only the 135 new spectra.

LDRs may be less impressive, there is extraordinary relative accuracy even though their sensitivity may be imagined to make them vulnerable to variability from, for instance, measurement artefacts including subtle possibilities such as stray light within the spectrograph (which is unexpected given the design of HERCULES and that our line-depths create ratios). Clearly our methods provide practically identical MLDR distributions of outstanding precision over nearly 20 yr, despite two CCDs being used and many other instrumental and environmental parameters varying as well. Thus we can be quite confident our LDRs are highly unlikely to be significantly compromised by any of these non-stellar variables.

We searched our data for periodicity using the generalized Lomb-Scargle (GLS) periodogram as derived by Zechmeister & Kürster (2009). The GLS is ideal for time series with uneven temporal sampling and nonuniform measurement errors as reported here. Our periodograms are normalized assuming the noise is Gaussian (Zechmeister & Kürster; their eq. 22). In Fig. 2, we show the result for our epoch-averaged MLDR temperatures, along with approximate analytical P -values estimated according to Sturrock & Scargle (2010). We find no evidence for statistically significant periodicity at any frequency.

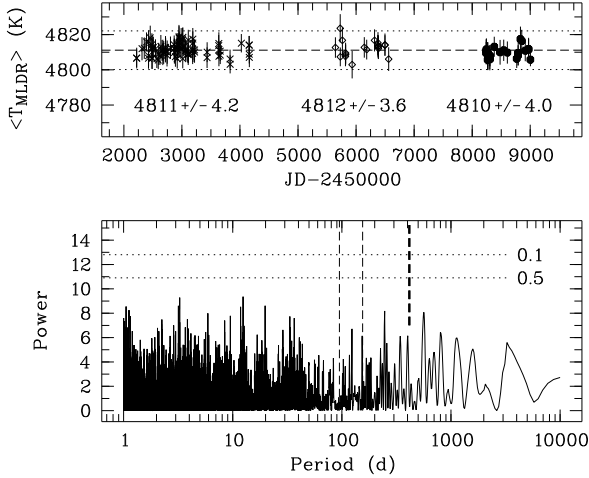


Figure 2. The 130 nightly means of the T_{MLDR} values from 398 LDR temperatures. Top: The distributions of the three LDR series defined in Fig. 1 together with their $\pm 1\sigma$ error bars. The mean temperatures $T_{\nu\text{Oct}}$ and their standard deviations are given below each series. Bottom: The Generalized Lomb-Scargle periodogram and corresponding FAP levels. The pair of vertical dashed lines identify our revised $\pm 1\sigma$ range of ν Oct A's predicted rotation period (see § 3.5). The shorter bold line marks the planet-like RV period ($P_{\text{RV}} \sim 415$ d).

3.3 Photometry from *Hipparcos* and TESS

We next make a brief digression to describe photometric satellite data which we will then compare to our LDR evidence. Since it has been estimated that ν Oct B is at least 6 mag fainter than ν Oct A (R09, and see Table 2), the LDRs and photometry are assumed to only record ν Oct A.

Two satellites observed ν Oct, acquiring data whose end dates are separated by 30.6 yr. The first, *Hipparcos*, achieved the longest baseline (~ 1176 d, 1989.45–1993.17; ESA 1997) and identified ν Oct A as one of its more stable targets (see Table 1). More recently, NASA's TESS mission (Ricker et al. 2015) observed ν Oct twice in the 2-minute short-cadence mode. It was covered in Sectors 13 (2019 Jun 19 – Jul 18) and 27 (2020 Jul 5 – Jul 30), i.e. baselines of about 28 and 24 days. We retrieved the Pre-search Data Conditioning Simple Aperture Photometry (PDCSAP) using the LIGHTKURVE software package (Lightkurve Collaboration, 2018). Approximately, this photometry has midtimes separated by 395 d and span 408 d. Therefore the two TESS records sample slightly different phases of the RV cycle (assuming $P_{\text{RV}} \sim 415$ d is still relevant), and together they include about 13 per cent of it. These high-precision records are also consistent with this bright spectroscopic binary being exceptionally quiet, at least during these short baselines and within TESS's spectral response capabilities (600–1000 nm bandpass; Ricker et al. 2015): the RMS scatter of each PDCSAP dataset and both combined is just 0.02 per cent.

3.4 Magnitude differences Δm_{LDR} from T_{MLDR}

The temperature calibration enables one more significant benefit: the T_{MLDR} values can be converted to a magnitude difference Δm_{LDR} using the Stefan-Boltzmann law ($L \sim R^2 T^4$). The *Hipparcos* and TESS photometry strongly support a claim that $\Delta L \sim 0$, and the LDR results just as strongly record $\Delta T \sim 0$.

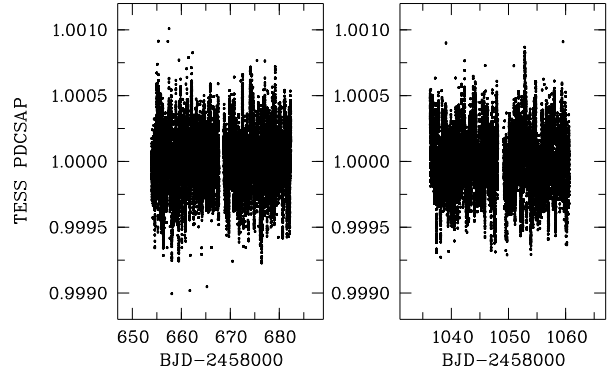


Figure 3. Two time series for ν Oct acquired by NASA's TESS mission during mid-2019 ($N = 19\,579$) and mid-2020 ($N = 16\,780$). The RMS of each data set is 0.02%. PDCSAP: Pre-search Data Conditioning Simple Aperture Photometry.

Therefore, though ν Oct A no doubt has some surface variability, as even less evolved stars do, we assume any radial changes are insignificant in our next calculation, a repeat of what was reported in R15 and R16. Eq. (1) provides the conversion to Δm_{LDR} with that assumption (i.e. $\Delta R = 0$):

$$\Delta m_{\text{LDR}} = -10 \log_{10} \left(\frac{T_{\star}}{T_{\nu}} \right) \pm \frac{10}{\ln(10)} \sqrt{\left(\frac{\sigma_{T_{\star}}}{T_{\star}} \right)^2 + \left(\frac{\sigma_{T_{\nu}}}{T_{\nu}} \right)^2}, \quad (1)$$

where we abbreviate $T_{\nu\text{Oct}}$ (i.e. 4810 ± 4 K) with T_{ν} . Note that Δm_{LDR} is extremely sensitive to the temperature: varying T_{\star} by only one degree changes Δm_{LDR} by about one millimagnitude.

In Fig. 4 we compare these Δm_{LDR} estimates to the magnitude differences for the longer baseline photometry of *Hipparcos*, whose Δm_{Hip} values relate to their mean. A striking similarity is evident between the four Δm distributions, all the more so as there are no zero-point offsets applied to any T_{MLDR} data. The latest MLDR series extends the time span of all Δm values to about 30.5 yr. This graph also demonstrates that the more recent lower- S/N data do not significantly compromise the precision of these Δm values relative to the earlier data sets.

Finally we note the small difference between the standard deviations of Δm_{Hip} and Δm_{LDR} , where $\sigma_{\text{Hip}} \sim 4.1$ is greater than $\sigma_{\text{LDR}} \sim 3.7$ mmag. Of the various possible reasons one perhaps more interesting to speculate is that this small difference records the anticipated tiny contribution that $\Delta R \neq 0$ would make to the *Hipparcos* photometry, but not our LDRs which are more directly sensitive to temperature changes. Our evidence for this is too slim for a credible claim but the idea might be successfully explored with more suitable data.

This completes our work with LDRs. It confirms past conclusions: ν Oct A continues to have a very thermally-stable photosphere, which is difficult to reconcile with surface variability as we presently understand its many variations. As discussed in considerable detail in the LDR work reported in R15, neither star spots nor pulsations are believable scenarios for creating the planet-like RVs in these circumstances. The same explanations there apply here.

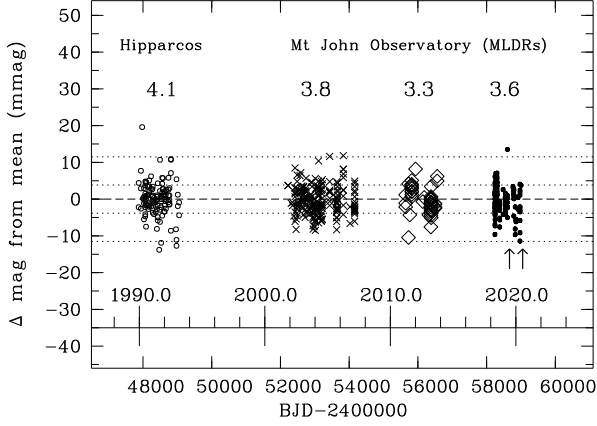


Figure 4. The 398 magnitude differences, Δm_{LDR} , derived using Eq. (1) and compared to Δm_{Hip} from 116 best-quality (flag = 0) *Hipparcos* observations. The value above each series is the standard deviation of Δm (mmag) weighted by the standard errors. The upward arrows identify the midtimes of the two TESS photometric baselines (2019, 2020).

3.5 *Gaia* and more clues negating a stellar origin for RVs

With the benefit of *Gaia*'s parallax (see Table 1) and our confirmation of the photosphere's stable temperature, we can also review several parameters that have some relevance here. The *Gaia* parallax is about 10 per cent greater than the three values reported in R09, which includes that from *Hipparcos* (ESA 1997). Consequently ν Oct A's luminosity is less, which we now estimate is about $14 L_{\odot}$ (and $M_V = +2.3$ mag; Table 1). Based on the weighted mean of the five temperatures given above (i.e. 4825 ± 21 K), ν Oct A's radius is also less i.e. $5.3 \pm 0.4 R_{\odot}$ (see R09, their eq. 3). The star is therefore now classified more closely as a subgiant, i.e. $\sim K1$ IV, and placed in a sparsely populated part of the H-R diagram (very near γ Cep A), well-separated from the so-called instability strip and other known classes of pulsating stars. It remains to be seen if future revisions change this significantly.

Such a star is not known to have a rotation period anywhere near as long as that of the RV cycle i.e. $P_{\text{RV}} \sim 415$ d. In fact, the star's $v \sin i \sim 2 \text{ km s}^{-1}$ (see Table 1), our revised estimate for the radius, and assuming the rotational and orbital axes are parallel, i.e. $i_{\text{rot}} \sim 71^\circ$, predicts the star's rotation period is $P_{\text{rot}} = 125 \pm 30$ d. R09 devotes their sec. 4.1.7 to the considerable improbability that rotation could be significant for the RV signal's origin. This scenario was made even more difficult to believe when R16 doubled the time span of the persistent RV cycle to 12.5 yr, and is reduced even further by the new evidence presented here.

Finally, we assess if solar-like oscillations have any chance of influencing our observations of the now less-evolved ν Oct A. One way is to apply the formulae from Kjeldsen & Bedding (1995), specifically equations 7, 8 and 10 to our new values for $[R, T_{\text{eff}}, L]$. Using the weighted mean for the stellar mass, $1.6 \pm 0.1 M_{\odot}$, such oscillations have a predicted velocity amplitude of about 2 m s^{-1} , a maximum-power period of only 1.5 hr and a luminosity amplitude $\delta L/L \sim 54 \text{ ppm}$ at 6000 \AA (the wavelength from Wein's Displacement Law for the peak luminosity for our mean T_{eff}). These values are in excellent agreement with the graphical ones in Dupret et al. (2009) who studied both radial and non-radial oscillations. One of their stellar models is slightly evolved and similar to ν Oct A (their

Case A, fig. 5, panel 3 at $\nu = 190 \mu\text{Hz}$). Its non-radial modes have smaller amplitudes than the radial ones, and together these produce a low-amplitude and very complex frequency spectrum, nothing like ν Oct A's planet-like RV signal. Such oscillations cannot have any significant impact on any of our data.

We now report our analysis of the chromosphere-activity indicators, the Ca II H line and H α , the study of which benefits from the long series of precise LDR results – any photospheric contribution to these indices is almost certainly insignificantly variable.

4 CHROMOSPHERE ACTIVITY: Ca II AND H α INDICES

Many spectral lines have been identified as being useful for monitoring chromosphere activity in late-type stars (see e.g. Lisogorsky, Jones & Feng 2019). One of the motivations for assessing such behaviour is the quest for increasingly precise RVs for exoplanet searches. Whilst many photosphere lines can be used as indicators for chromosphere activity, the classic ones with the strongest history are the resonance doublet lines of Ca II H and K at 3968.47 and 3933.66 \AA close to the boundary of the ultraviolet and visible (see e.g. Wilson 1963; Linsky & Avrett 1970; Wilson 1978; Duncan et al. 1991; Baliunas et al. 1995). However, these two lines have the weakness, which will significantly influence our study, that they are recorded in spectral regions that have inherently low S/N .

At the other end of the visible spectrum is H α (6562.808 \AA). This has the distinct advantages of much higher S/N than provided at Ca II H and K ($\sim 4 - 5 \times$ greater), and a better defined continuum without the complications of many neighbouring metal lines as Ca II H and K also have. However, as we will show, H α instead has the complication of telluric lines, and for a quiet star such as ν Oct A, these lines dominate the line-index variability. The S/N differences resulted in our having a final set of about 200 Ca II H-line indices but nearly six times as many H α indices.

4.1 Line index definitions including covariance

An index is a conventional method to assess variability of a suitable line's core for evidence of stellar activity (for its earlier history see Griffin & Redman 1960). Our index, I , includes the line's core interval F_0 and two reference intervals F_1 and F_2 :

$$I = \frac{2 \times F_0}{F_1 + F_2}, \quad (2)$$

where each flux interval i comprises N_i bins having relative fluxes f_i . Modern studies use either total fluxes or mean fluxes: the index derived from mean fluxes $\langle F_i \rangle$ exceeds that from total fluxes by N_R/N_0 (if $N_R = N_1 = N_2$). If total fluxes are used, the error on each flux $\epsilon_i = \sigma_i \times \sqrt{N_i}$. If mean fluxes are used $\epsilon_i = \sigma_i/\sqrt{N_i}$, i.e. the standard error on the mean, which ensures the index's relative error will be identical to that from total fluxes. We will always use mean fluxes.

The index error ϵ_I was calculated using error propagation:

$$\left(\frac{\epsilon_I}{I}\right)^2 = \left(\frac{\epsilon_0}{F_0}\right)^2 + \frac{\epsilon_1^2 + \epsilon_2^2}{(F_1 + F_2)^2} = E_1 + E_2, \quad (3)$$

where we introduce the error symbols E here and below for future reference. Whilst this is the typical calculation for such an index, Eq. (3) may be incomplete since the flux errors are calculated from

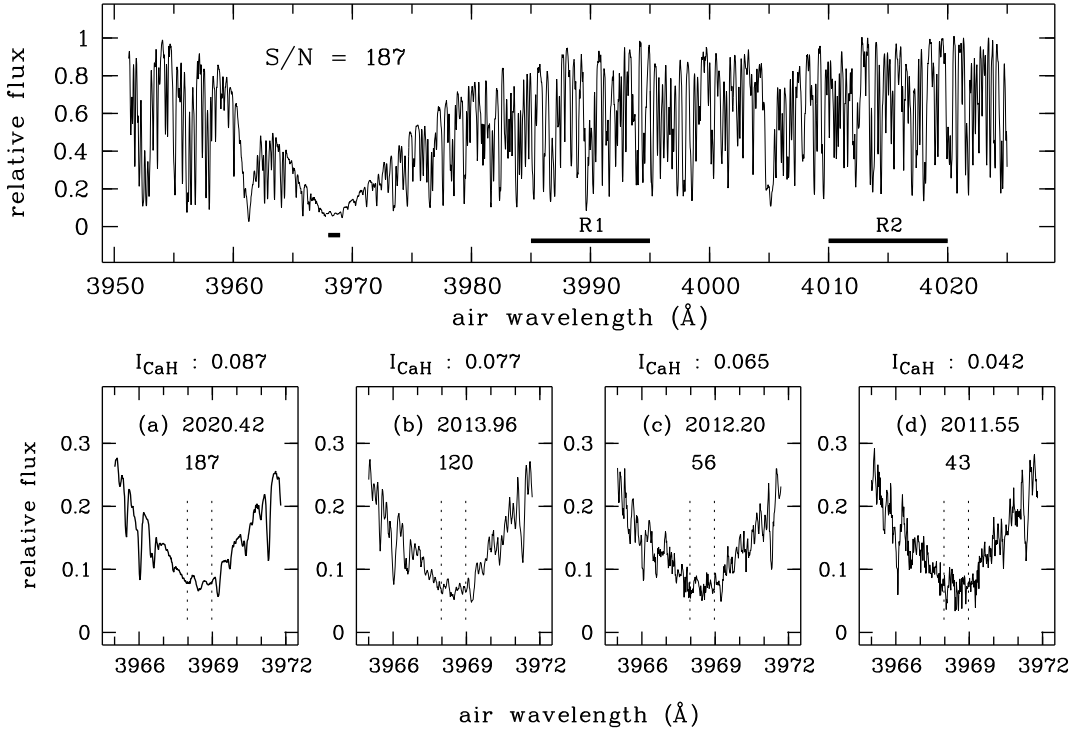


Figure 5. Four ν Oct A Ca II H-line spectra for representative epochs, preliminary indices and S/N values. In each plot the core width represented is 1.0 \AA . Top: The highest S/N spectrum across three orders. The core width and two reference intervals are marked with bold horizontal lines. The core is magnified below in (a). Below: The cores of four spectra with both decreasing S/N and index I_{CaH} . Included are the I_{CaH} , observation date, and S/N .

the fluxes which, if suitably chosen, should be highly correlated. This suggests covariance deserves consideration.

The expression for the total covariance CoV must be added to Eq. (3):

$$CoV = -\frac{2\epsilon_0\epsilon_T}{F_0(F_1 + F_2)}\rho_{0,T} + \frac{2\epsilon_1\epsilon_2}{(F_1 + F_2)^2}\rho_{1,2} = E_3 + E_4, \quad (4)$$

where ρ is a correlation coefficient, T represents the sum of the reference fluxes, and ϵ_T is calculated by also including its covariance term, i.e.,

$$\epsilon_T = \sqrt{\epsilon_1^2 + \epsilon_2^2 + 2\epsilon_1\epsilon_2\rho_{1,2}}. \quad (5)$$

The sign of $\rho_{0,T}$ and $\rho_{1,2}$ will determine if E_3 and/or E_4 increase or decrease the total error, or if $E_3 + E_4 \rightarrow 0$. If only one reference interval is used and covariance taken into consideration, the contribution of E_4 to the total error is absent.

4.2 Ca II H line spectra and data set

When seventeen Ca II H-line indices were reported in R16, the spectra we analyse here were available. However, most of the 700 archived Ca II spectra, have quite low S/N ($\lesssim 60$), and previously had been considered probably useless for any definitive study based on expectations and a preliminary sample's analysis.

As a definitive understanding of the ν Oct system is yet to be

attained, we took a second look at this large pool of spectra to review the earlier decision. We decided that it was a poor strategy to co-add spectra since the few available for most nights result in very little advantage and co-adding many across multiple epochs would provide fewer final indices, most obtained with greater complication and risk for errors as for instance Zechmeister et al. (2018) warns. Instead, a rather more novel approach was undertaken when a distinctive distribution that could be modelled revealed itself from a larger sample of indices.

The HERCULES archive provided an initial sample of 482 spectra. Many of the original 700 spectra could not be properly processed due to more prevalent cosmic rays and other complications. We restricted our analysis to the record of the Ca II H line in $n = 143$ as its S/N is about 40 per cent greater than its duplicate in $n = 144$ and both records of Ca II K. The 218 discarded spectra have $S/N \lesssim 30$ at the H line record we used. Four H-line spectra of varying S/N are illustrated in Fig. 5 showing ν Oct A's minimal chromospheric activity and the extent of slight infilling which varies primarily due to spectral noise.

4.2.1 Preliminary Ca II indices and errors

The origin of the dominant chromospheric flux is in the vicinity of the temperature minimum (Linsky & Avrett 1970) which is presumably highly correlated with the LDR temperatures just described. The Ca II H line has variable amounts of infilling and activity depending on, for instance, the star's luminosity (Wilson & Bappu 1957). Typically the Ca II H-line core of main-sequence stars is sampled with an interval of about $1\text{--}1.1 \text{ \AA}$ (e.g. Wilson

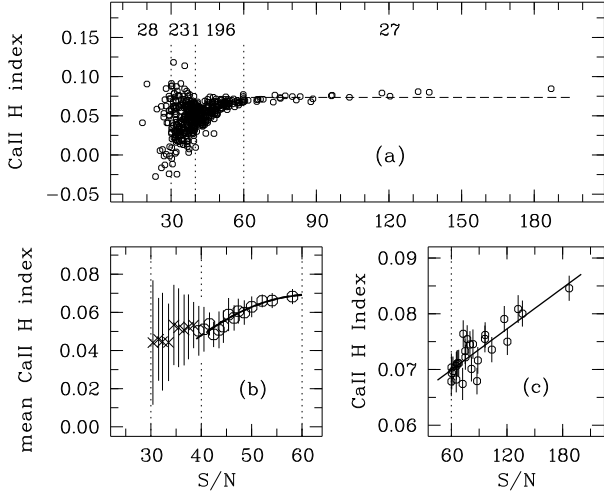


Figure 6. The preliminary Ca II H indices from 482 ν Oct A spectra for a core width $W = 1.0 \text{ \AA}$. (a) The indices, with the total for each subset bounded by $S/N = 30, 40, 60$ given above. The dotted horizontal line identifies the weighted mean for the 27 spectra with $S/N \geq 60$. (b) The weighted mean indices for each $\langle S/N \rangle$ bin. The bold curve is the parabolic fit to the 13 $\langle S/N \rangle$ bins in the range $[39, 60]$. (c) The linear fit for $S/N \geq 60$. In (b) and (c) the y-scale is magnified for clarity and the vertical solid lines represent $\pm 1\sigma$.

1978; Duncan et al. 1991; Cincunegui et al. 2007; Boisse et al. 2009). The residual photospheric contribution which complicates accurate measurements of only the chromospheric component, for instance for surveys with different spectral types and luminosity classes (see e.g. Oranje 1983; Rutten 1984) can be neglected here since we are studying only ν Oct A, which in any case has a very thermally-stable photosphere from evidence summarized in Fig. 2.

Our H-line cores have a width of about 1.0 \AA ; see Fig. 5. This detail provides further indirect evidence for ν Oct A’s revised less-evolved luminosity class (see § 3.5). Rather than commit to a single interval width W we used a series in 0.1 \AA steps from 0.9 \AA to 1.5 \AA . We selected two reference intervals, R1 and R2, each 10 \AA wide, centered at $\lambda_{\text{air}} = 4015 \text{ \AA}$ in order $n = 142$ and at $\lambda_{\text{air}} = 3990 \text{ \AA}$ in order $n = 143$ (see top panel Fig. 5). The second redder reference interval was chosen so that it would have a slightly higher S/N motivated by our mostly low-quality spectra.

Our preliminary 482 indices are shown in Fig. 6(a), given in relation to their S/N . These distributions fall into four ranges delineated by the vertical dotted lines in each panel at $S/N = 30, 40$ and 60 . In Fig. 6(a) the anticipated near constancy of the indices for a quiet star such as ν Oct A is evident for $S/N \geq 60$. The distributions of $E_1 \dots E_4$ and their sum are illustrated in Fig. 7. Our errors yield $\rho_{0,T} \sim -0.2$ and $\rho_{1,2} \sim +0.7$, so that both E_3 and E_4 are positive, and E_3 is about as significant as E_4 . E_1 is always the dominant term, but its contribution decreases as S/N increases. The error terms tend to plateau just above the threshold $S/N \sim 60$, particularly for E_3 and E_4 . Below this threshold, the total error increases exponentially (Fig. 7b), and above it, the minimum errors begin and average 0.0024 ± 0.0002 . This error, incorporating the covariance terms, is equivalent to about 3.4 per cent of the index and about $2.5\times$ greater than the error without covariance included, a significant difference.

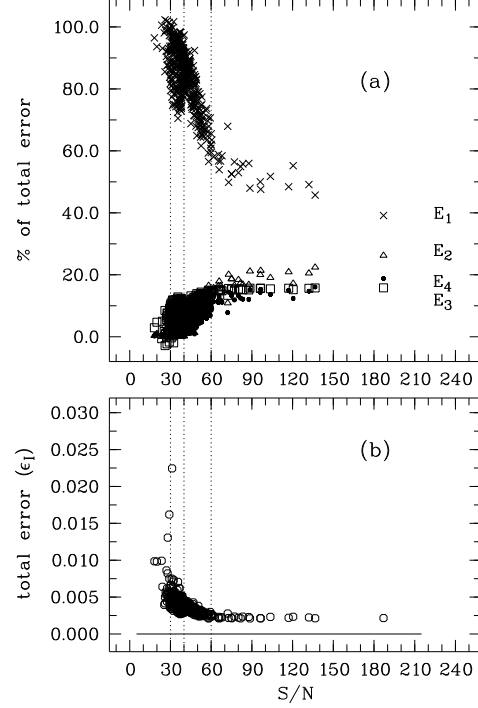


Figure 7. The preliminary Ca II H index errors from 482 ν Oct A spectra. (a) The percentage fraction each error term contributes to the total. The single isolated symbols label the values from mid-2020 (JD245 9002). The three dotted vertical lines are as in Fig. 6. The errors are for a core width $W = 1.5 \text{ \AA}$ since narrower widths have E_2, E_3 and E_4 increasingly coincident, approaching a mutual minimum contribution of about 10 – 15%. (b) The total errors given by the sum $E_1 + E_2 + E_3 + E_4$.

4.2.2 Modelling the trends in Fig. 6(b) and (c)

The apparently near-constant 27 indices with $S/N \geq 60$ in Fig. 6(a) in fact delineate a fairly well-defined sloping line as shown below in Fig. 6(c), even without the high- S/N anchor. This we modelled with a linear fit weighting each index by $1/\epsilon_1^2$ to give our modified indices:

$$I' = I - (a_1 S + a_0) + \langle I_{60+} \rangle, \quad (6)$$

where S represents S/N and $\langle I_{60+} \rangle$ is the weighted mean of these 27 indices and defines our zero-point for I' . Note that if our spectra had S/N limited to $[60, 90]$ the implied slope of the distribution $S/N \geq 60$ would disappear. The modelled indices have larger errors determined by the rescaled original index error created by the fitting process, the RMS of the linear fit (which varies with the core width of the H line), and the standard deviation of the original mean $\sigma_{\langle I_{60+} \rangle} = 0.004$, each added in quadrature.

It is impossible to guess what the average behaviour of the 427 indices is in the interval $[30, 60]$ in Fig. 6(a), so we created a series of narrow S/N bins, typically with $\Delta S/N = 1$. Starting at $S/N = 30$ we extended the $\Delta S/N$ range in one unit steps until we had at least ten indices in each bin. This provided 23 bins. For each bin we calculated the average and standard deviation of the S/N and the indices, each index weighted by its error as above.

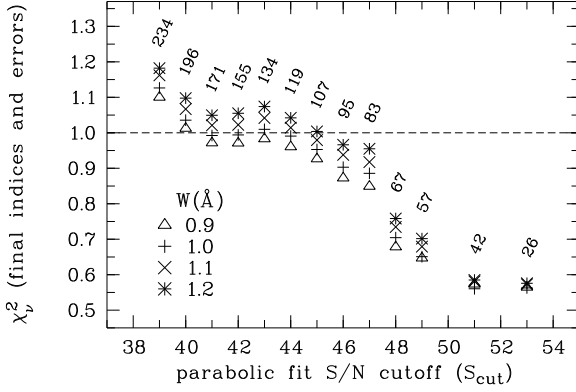


Figure 8. χ^2_{ν} values from our final indices and errors in terms of S_{cut} . The results for four Ca II H-line core widths W are shown. The number above each S_{cut} is the total number of indices included in each parabolic fit (shown in Fig. 6 b), these finally combined with the 27 high- S/N indices.

These statistics, in relation to each bin's mean S/N are plotted in Fig. 6 (b).

For $S/N \geq 39$ the indices are adequately fit by a parabola. This fit though requires further care as it is not obvious what is its lower limit, which we label as S_{cut} . Its choice is another balancing act between precision and sample size for our final time series since the binned indices have increasingly higher standard deviations as S/N decreases. We discarded 221 spectra in ten bins with $S/N < 39$ as they have the largest standard deviations and are least consistent with our intended parabolic fit (marked with crosses ‘ \times ’ in Fig. 6 (b)). For the 13 remaining $\langle S/N \rangle$ bins, which include 261 original indices, we calculated the model-fitted final indices and their errors for core widths of $W = [0.9, 1.2]$ Å. These four widths encompass those considered most suitable for our spectra (i.e. 1.0 and 1.1 Å; see Fig. 5).

4.2.3 Final indices and errors and their χ^2_{ν}

Of the original 700 archived spectra, ~ 60 per cent are discarded from our complete analysis which somewhat vindicates the decision several years ago. Our errors and indices are now final. The errors each comprise two conventional terms E_1 and E_2 , two covariance terms E_3 and E_4 and three terms from each model depending on the spectrum's S/N , making a total of seven terms. Each error is approximately doubled by the model-fitting calculations.

We calculated χ^2_{ν} for our final indices and errors for our grid of four H-line core widths and thirteen S_{cut} values. Fig. 8 shows that our atypical analysis of mostly low- S/N spectra and the inclusion of covariance ultimately provides strong evidence for the consistency of our indices, errors and models. For example, for the H-line core width $W = 1.0$ Å, $\chi^2_{\nu} \approx 1.0$ for the four consecutive parabolic fit thresholds $S_{\text{cut}} = [41, 44]$. Without covariance $\chi^2_{\nu} = 2$. Our final relative errors average about seven per cent for the 198 indices defined by $S_{\text{cut}} = 41$. In Fig. 9 we illustrate our final indices and errors for the time series defined by $S_{\text{cut}} = 41$ and $W = 1.0$ Å which corresponds to $\chi^2_{\nu} = 0.99$. This example is approximately normally distributed as the lower two panels illustrate. We also derived $\chi^2_{\nu} = 0.99$ for the 27 indices from the spectra with $S/N > 60$.

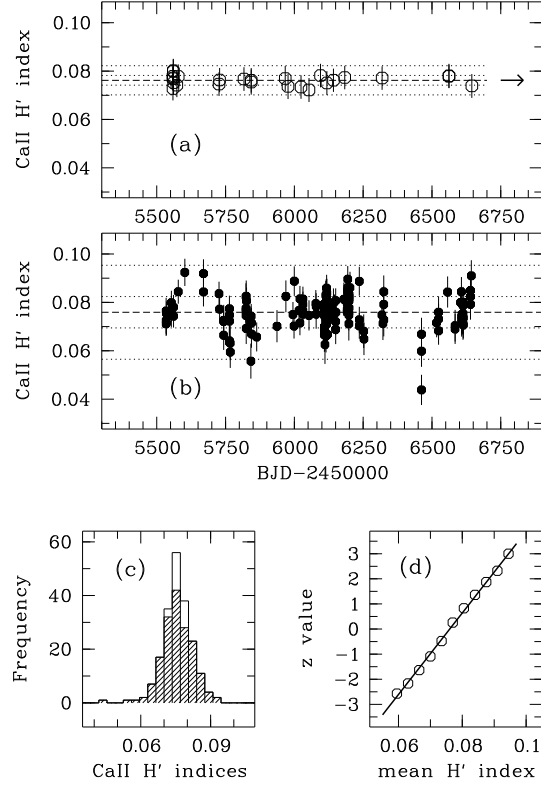


Figure 9. Two distributions of indices based on the Ca II H-line core width $W = 1.0$ Å. Top panels: The dashed and dotted horizontal lines identify the mean and ± 1 and $\pm 3\sigma$. The error bars are $\pm 1\sigma$ and the y-scales are identical. (a) 27 indices with $S/N > 60$, $\chi^2_{\nu} = 0.99$. The right arrow points to the mid-2020 (JD245 9002) index. (b) 171 indices with $S/N \geq 41$, $\chi^2_{\nu} = 1.06$. (c) Frequency distribution of 198 indices. Open: (a) indices. Hashed: (b) indices. (d) Normal probability plot of 196 indices within $\pm 3\sigma$ of the mean in (b), and the regression line based on the index mean and standard deviation.

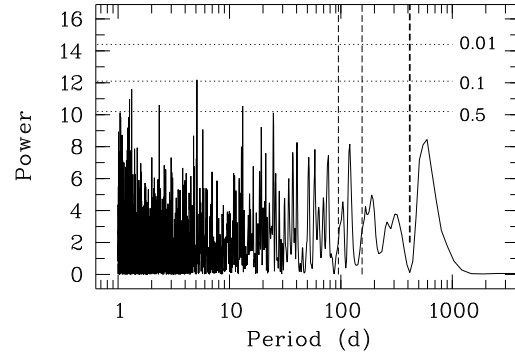


Figure 10. GLS periodogram of the final series of 198 H-line indices using $S_{\text{cut}} = 41$, with the corresponding FAP levels. The pair of vertical lines identify the boundaries of our revised predicted $\pm 1\sigma$ range of ν Oct A's rotation period (see § 3.5) and the bolder line the planet-like RV period ($P_{\text{RV}} \sim 415$ d).

As we found with our LDR work, within our errors, there is nothing here that suggests anything but quite randomly distributed data, regardless of the temptation to perhaps imagine some significantly periodic behaviour in Fig. 9 (b) where removal of only a very few data points would make such a suspicion far less likely. Our GLS periodogram search as described in § 3.1 confirms this (see Fig. 10). It was created using the indices plotted in Fig. 9. There is no significant peak corresponding to ν Oct A's predicted rotation period ($P_{\text{rot}} \sim 125$ d) or the planet-like RV period ($P_{\text{RV}} \sim 415$ d) where a deep trough is in fact evident. Unfortunately, our lack of any detection of a credible rotation period (both here and with our LDR data) means we are still limited to estimates of P_{rot} as in Table 1 and § 3.5 (where, in any case, we noted rotation remains a highly unlikely explanation for the RV cycle).

4.3 H α spectra and data set

ν Oct A's unique planet claim demands certainty about any conclusions relating to any index variability similar to the RV signal. Our H α indices have this characteristic, having a quasi-periodicity in the vicinity of the conjectured planet's period. We intend to provide robust proof that this is caused solely by telluric lines.

H α is a prominent photospheric absorption line in late-type stellar spectra. Its core can also include chromospheric activity. It was this profile variability that led to H α being studied for β Cephei in 1979 using one of the first digital detectors, an experimental Fairchild CCD (Young, Furenlid & Snowden 1981).

We employed a long time series of H α indices as densely sampled as possible, corresponding to the I₂-cell RVs reported in R16. Such a sample is critical for demonstrating the cause of the dominant variability in our indices. The 1160 spectra archived over four years comprise 229 epochs. Thirty spectra (from 18 epochs) were acquired without I₂ which are useful to compare our indices with and without I₂ involvement. For the majority with I₂ lines, our I₂ cell benefited from a temperature controller designed to minimise variability (50.0 ± 0.1 C), so that the density and extent of the I₂ forest was assumed to be quite constant.⁵ H α is recorded in two HERCULES spectral orders, $n = 86$ and 87 . The S/N in order 87 is about twice that in 86 so we used only $n = 87$, their range at H α being $S/N \sim [90, 570]$ and their mean 220.

Our first evidence of the role of telluric lines is presented before indices are calculated. The high S/N region where H α resides is also uncomplicated by large numbers of other photospheric lines such as the metal lines near Ca II H and K. It is therefore very suitable for making a preliminary visual comparison of all of our spectra with respect to a reference. This has the advantage that the entire H α region can be assessed for significant flux variations which may be concealed by the solitary line index. We ensured all our spectra have an essentially level continuum with a maximum relative flux $f_{\text{max}} = 1.0$, and that each H α core centre is measured accurately to within a pixel by also comparing the fitted centre of the sharp Ca I line (~ 6572.8 Å) redward of H α with each H α core fit. We calculated the relative flux differences Δf_i between each spectrum and our reference (see Fig. 11).

This plot alone is strong evidence that H α has very little core activity since the Δf_i variations for the core interval $[-15, +15]$ km s⁻¹ are actually the least of the wide range shown. Instead we see time-dependent line movement contaminating both

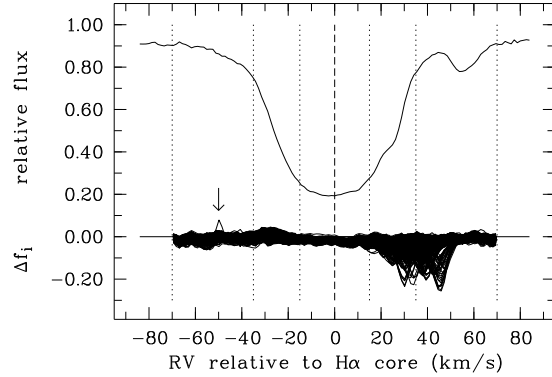


Figure 11. 1160 H α flux-difference curves (Δf_i) relative to the ν Oct A reference spectrum plotted above. The core boundaries of our H α indices are identified with dotted vertical lines at $[-15, +15]$, $[-35, +35]$, and $[-70, +70]$ km s⁻¹. The small arrowed feature is likely to be due to a cosmic ray since it does not appear in the duplicate record in order 86.

shoulders of H α , but particularly the redward one, which subsequent evidence will prove are telluric lines. We were fortunate that the strongest telluric lines did not engulf our line cores as may occur in other circumstances.

4.3.1 Non-stellar lines and ν Oct A's absolute RV

All of our spectra include telluric lines and most also the I₂ forest. An example of these non-stellar lines in a HERCULES spectrum of the fast-rotating Be star Achernar (α Eri, B6V, $v \sin i \sim 250$ km s⁻¹) is provided in Fig. 12. About a dozen prominent telluric lines are recorded but the H α region includes many more fainter ones.⁶

ν Oct A's absolute RV is intimately connected to the relative behaviour of its lines and any non-stellar lines. We measured the absolute radial velocity (RV_{abs}) of ν Oct A using the shift from the rest wavelength of the Ca I line at ~ 6572.8 Å. This line is recognized for its relative stability (e.g. Kürster et al. 2003; Robertson et al. 2013), and for our purposes, the resulting low-precision RVs are adequate. Our RV_{abs} estimates and the best-fitting curve are provided in Fig. 13. Vertical lines identify the RV minima which have different time spans Δt between them making them ideal for connecting the RV_{abs} variations to our index variations that we will next describe. Note that all of the Δt intervals differ from the orbital period of the conjectured planet and the predicted rotation period of ν Oct A, and critically, the Δt differences are due to ν Oct A's orbital RVs that a single star would not provide.

Fig. 14 includes the H α spectrum with the highest S/N , a cartoon representation of the strongest telluric lines recorded in Fig. 12, and identifies the Ca I line. The reference intervals R1 and R2 are defined in the next section.

⁵ We will discuss the absence of any significant impact of the I₂ forest on our H α indices in the final paragraph of § 4.3.2.

⁶ For instance, within the 95 Å shown in Fig. 12, the online database HITRANonline (<https://hitran.org>) lists 576 water vapour lines, the principal species contributing to the telluric spectrum. For details of its latest release see Gordon et al. (2017).

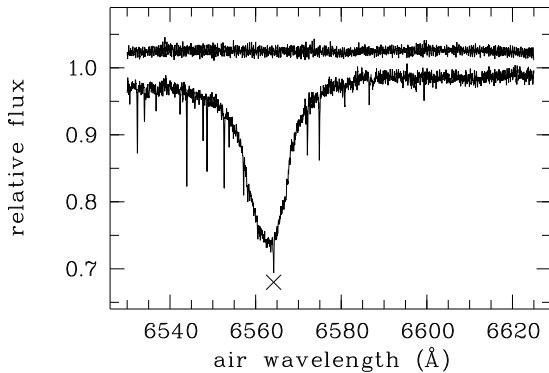


Figure 12. Above: the weak but dense I₂-line forest in the vicinity of H α (from a white+I₂ spectrum). Below: A spectrum of the fast-rotating α Eri (B6V, $v \sin i \sim 250 \text{ km s}^{-1}$) including I₂ and about 15 more prominent telluric lines. The wavelength range is about 25 \times greater than the equivalent of the RV scale in Fig. 11. The telluric line marked with ‘x’ ($\sim 6564.2 \text{ Å}$) also dominates the redward shoulder of the Δf_i curves in Fig. 11.

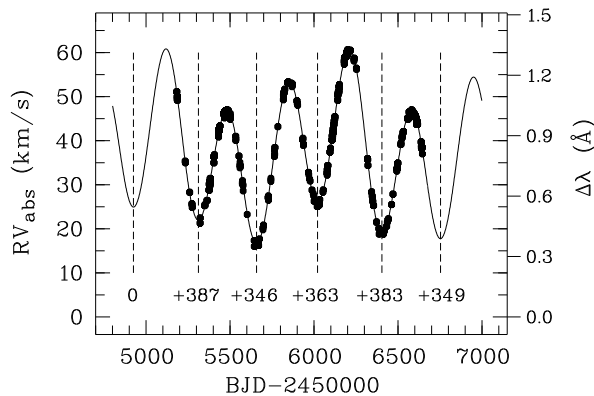


Figure 13. The absolute radial velocity of 1160 ν Oct A spectra based on the wavelength shift $\Delta\lambda$ of the Ca I line at $\lambda_{\text{air}} = 6572.8 \text{ Å}$. The vertical dashed lines mark successive RV_{abs} minima with the time interval Δt to the integer day between them (their average is 365.6 d). The curve is based on the barycentric RV corrections ($\sim [-16, +16] \text{ km s}^{-1}$) and the orbital solutions for ν Oct A and the conjectured planet (Ramm et al. 2016), and our best-fitting estimate of the systemic RV ($+37.4 \text{ km s}^{-1}$).

4.3.2 H α indices

The literature describes many choices for the flux intervals for H α indices. For a survey of their variety see e.g. Kürster et al. (2003); Cincunegui et al. (2007); Gomes da Silva et al. (2011); Ortiz et al. (2016); Zechmeister et al. (2018). We used three H α core widths, with the centre defining the RV zero-point for all flux intervals. The narrowest, $[-15, +15] \text{ km s}^{-1}$, is suggested by the evidence in Fig. 11, and is similar to that used by Kürster et al. (2003). We also included the wider interval $[-35, +35] \text{ km s}^{-1}$ (similar to Zechmeister et al. 2018) and one twice that, $[-70, +70] \text{ km s}^{-1}$, chosen to be just beyond the maximum absolute RV of ν Oct A ($\sim 61 \text{ km s}^{-1}$). We used the two reference intervals R1 and R2 defined by Zechmeister et al. (2018), namely $[-300, -100] \text{ km s}^{-1}$

and $[+100, +300] \text{ km s}^{-1}$ and calculated the index errors including covariance as described earlier.⁷

Unlike our Ca II indices, there is no correlation between S/N and our H α indices ($\rho \sim +0.08$). However, none of the index distributions (see Fig. 15) appear to be strictly random – they all have evidence of cyclic behaviour with the dominant period of about one year, although this doesn’t become better defined until the index uses the two wider H α regions, the main reason for their inclusion. Only the widest core width provides a significant maximum peak power in a periodogram and this is at 365.5 d (coincidentally the mean of the approximated RV_{abs} timespans in Fig. 13 is 365.6 d). This quasi-periodicity close to one year strongly implies the primary cause has a non-stellar origin, i.e. telluric lines.

For the first time we demonstrate the usefulness of the five RV_{abs} minima lines as evidence that telluric lines are the dominant cause of our index variations: the set of lines has been offset in time by -90 d for the $[-35, +35] \text{ km s}^{-1}$ core width but unadjusted for the widest one, and these included in Fig. 15 for the top two panels. Not only is adequate alignment found, simply made by eye, but the two offsets are unequal. The relative contributions of stellar and telluric lines vary if the flux intervals differ and this explains why the time shift to make this alignment is unequal for the two wider core widths that we can more easily assess – in fact, for this reason, it is also more likely the shifts will differ. The more precise index variations of the widest core interval is perhaps explained by the more prominent roles of both the very stable photosphere and the additional telluric lines found here (which are also present in the reference intervals).

Thirty spectra were acquired without the I₂ cell, the benefit of which is also clear from Fig. 15: the no-I₂ indices have a distribution that is consistent with those with I₂. To confirm this similarity, we also derived indices from our 135 new spectra (used for our LDR study) whose spectra also have no I₂ lines. Their distribution is far less dense and uniform than our much larger series (which is the principal reason the former were not otherwise included for H α) but are statistically indistinguishable from that derived from spectra with I₂. This demonstrates that the previous concern for using spectra including the I₂ forest for an H α study was unfounded, and duplicate the claim made in Kürster et al. (2003) that I₂ involvement made no significant impact on their H α and Ca I indices for Barnard’s star. That the complete absence or inclusion of I₂ lines makes no significant difference to these indices also makes it clear that any temperature variations of the I₂ cell leading to variability of the forest’s extent is highly unlikely to make any difference either.

4.3.3 Other evidence

Several more pieces of evidence ensure our H α variations are dominated by telluric lines. Firstly, Bergmann (2015) used HERCULES to also measure H α indices for τ Cet, δ Pav and α Cen A and B in the same time span and frequently on the same nights as our ν Oct A spectra. These indices use a wider core interval $[-115, +115] \text{ km s}^{-1}$ and different reference intervals but still

⁷ We also calculated all of our indices using the reference intervals defined by Kürster et al. and Cincunegui et al., which are distinctly different from Zechmeister et al. These index distributions were indistinguishable for the narrowest core width and barely so for the mid-width core. The indices we derived with the Zechmeister et al. reference intervals were significantly more precise for the widest core interval, which is why they are reported.

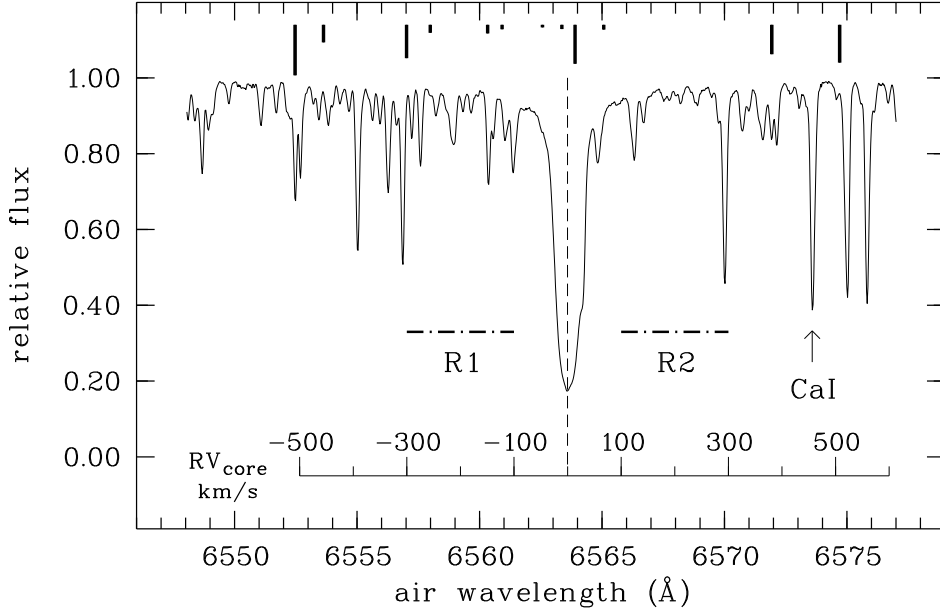


Figure 14. The $H\alpha$ region of our ν Oct A spectrum with the highest $S/N \sim 570$. It has $RV_{\text{abs}} \sim +35.9 \text{ km s}^{-1}$ which coincidentally is about midway in the range of RV values depicted in Fig. 13. The core centre is marked with a vertical dashed line at $RV_{\text{core}} = 0$ and our two reference intervals R1 and R2 located accordingly. The stellar spectrum and RV_{core} scale will move relative to the wavelength scale due to RV_{abs} , whereas the cartoon of telluric lines above the spectrum is fixed. Note this spectrum’s Ca I line is bounded by two strong telluric lines separated by $\sim 130 \text{ km s}^{-1}$ and is discussed in § 4.3.3.

those distributions and ours are very similar. Bergmann’s four stars and ν Oct A all have similar RV_{abs} ranges ($\sim 45 - 55 \text{ km s}^{-1}$) so all had $H\alpha$ moving relative to telluric lines in quite similar ways. Secondly, Bergmann’s strategies to manage stray-light contamination between α Cen A & B were strictly defined by his evidence his distributions were also substantially due to telluric line involvement, and more specifically, water vapour. Thirdly, Bergmann’s reduction pipeline differed from ours so the chances of the two duplicating a reduction artefact is also highly unlikely.

The final evidence comes from indices of the recognized ‘stable’ Ca I line used for our absolute RV estimates. We also calculated these using a series of core widths: the $[-15, +15] \text{ km s}^{-1}$ interval that is very similar to that used by Kürster et al. and Robertson et al. (2013) for their Ca I indices, and a series in 10 km s^{-1} steps from $10-70 \text{ km s}^{-1}$. We found $[-30, +30] \text{ km s}^{-1}$ provided the least variation (half that provided by $[-15, +15] \text{ km s}^{-1}$). Again, the core interval $[-70, +70] \text{ km s}^{-1}$ recorded most distinctly the influence of telluric lines (see Fig. 16). Note that this wider interval is more than the separation of the two strong telluric lines bounding Ca I in Fig. 14, and so both influence some Ca I indices. Our RV_{abs} minima lines are again successfully aligned to the dominant cycles for the wider core interval. These results show that 1. the index distribution of the stable Ca I line closely mimics our $H\alpha$ indices and has the least variation of all our indices (the mean for $[-30, +30] \text{ km s}^{-1}$ is $0.958 \pm 0.003 \equiv 0.3 \text{ per cent}$), and 2. if confirmation of stability is desired, Ca I or any other line is best studied when less likely to be contaminated by tellurics.

4.3.4 $H\alpha$ index errors and final comments

We calculated our index errors $E_1 \dots E_4$ using the same methods described in § 4.1. Given the significant impact of the covariance terms E_3 and E_4 to our Ca II index errors, it was somewhat surprising that they make little difference to our $H\alpha$ errors, since the mean fluxes of the reference intervals are again highly correlated, just as they were for our Ca II indices ($H\alpha$: $\rho_{1,2} \sim 0.9$). However, perhaps related to the influence of telluric lines, the associated errors ($\epsilon = \sigma/\sqrt{N}$) are not at all highly correlated, regardless of the core or reference intervals used, since we also checked this result with the Kürster et al. reference intervals. If this result is common in other $H\alpha$ index studies it shows that the absence of the covariance terms also made no significant difference to their errors.

The core width that is most suitable for our original purpose – assessing $H\alpha$ ’s activity – is the narrowest one, $[-15, +15] \text{ km s}^{-1}$. That index distribution is in the bottom panel of Fig. 15. E_1 is again by far the dominant error term. The relative contributions of the four error terms to their total are (0.962, 0.046, 0.005, -0.013). The relative total errors have a mean $2.3 \pm 0.3 \text{ per cent}$ which yield $\chi^2_\nu = 0.9$. Both E_3 and E_4 are practically zero for two different reasons: $E_3 \sim 0$ as $\rho_{0,T} = -0.016$, and $E_4 \sim 0$ primarily because the error portion is ~ 0 (and $\rho_{1,2} = -0.30$, so that E_4 actually reduces the total error, but only insignificantly).

That we can precisely correlate the tiny effects of telluric lines in terms of RV_{abs} suggests our methods are reliable and any $H\alpha$ activity is likely to be significantly less. Also, as a final minor detail, having established the origin of the dominant variations, we can now speculate that contributions to the almost nightly variations may be differences with the observations’ airmasses and the hu-

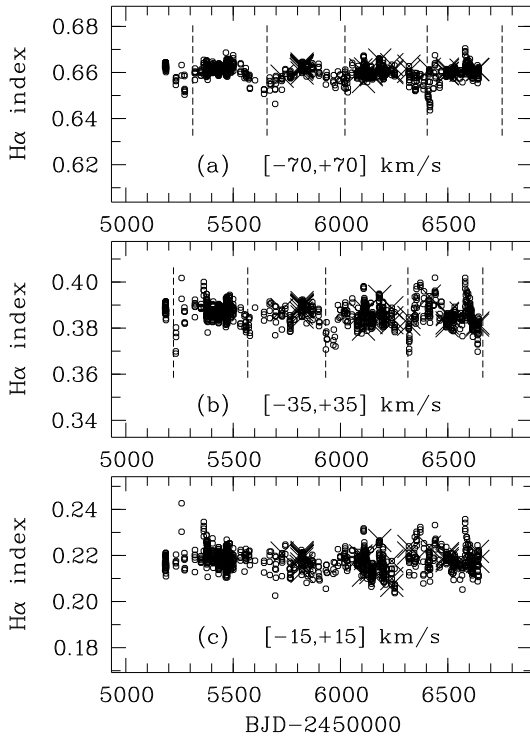


Figure 15. $H\alpha$ line indices from 1160 ν Oct A spectra for three core intervals. ‘o’: 1130 indices with I_2 , ‘x’: 30 indices without I_2 . (a) The dashed vertical lines are unshifted relative to their zero-point time in Fig. 13, but in (b) are shifted by -90 d, so these two 5-line sets are offset from each other. The y-axes all span the same range i.e. 0.085. The mean percentage errors for the ± 15 , ± 35 and ± 70 km s^{-1} indices are respectively 2.3 ± 0.3 , 6.9 ± 0.2 and 4.5 ± 0.05 per cent.

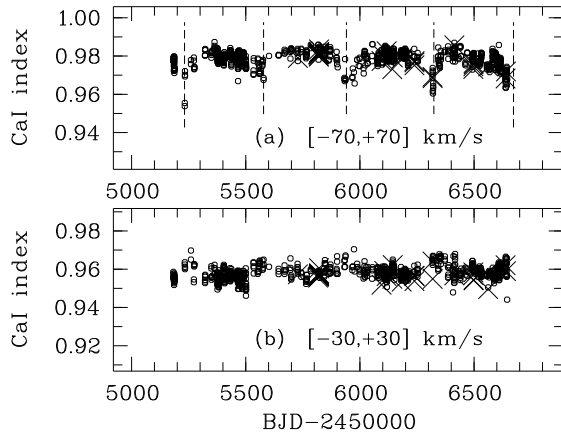


Figure 16. Ca I indices from 1160 ν Oct A spectra for two core widths. ‘o’: 1130 indices with I_2 , ‘x’: 30 indices without I_2 . The axis ranges are as in Fig. 15. The dashed vertical lines in (a) are shifted relative to their zero-point in Fig. 13 by -80 d.

midity that the telluric lines’ primary component, i.e. water vapour, also records.

5 CONCLUSION

We report five new independent series of precise data that all indicate ν Oct A is a very quiet star: two photometric series from TESS (2019, 2020), which more or less coincide with our LDR study of its photosphere (2018–2020), and our two large surveys of its chromosphere whose origin is the I_2 -cell RV time series (2009–2013). The TESS photometry bounds the 1437 RVs (2001–2013) with *Hipparcos* observations three decades before (1989–1993). A sixth line of new evidence is the *Gaia* parallax that indicates ν Oct A is less luminous, and so more probably approximately K1 IV. This also strongly favours the quiet-star classification, as does our review of solar-like oscillation scenarios. These results are consistent with all previous surveys, for instance, more recently, two bisector studies (R09 and R16), and two other LDR studies (R15 and R16).

There is no significant variability of any of these many photometric or spectroscopic time series, and certainly none correlated with the planet-like RVs. Other facts are against ν Oct being a hierarchical triple-star system or the cause being related to ν Oct A’s rotation. Thus this overwhelming evidence demonstrates all non-planetary solutions continue to be implausible, which instead we interpret is only compatible with a retrograde planet whose properties are approximated in Table 2.

With thousands of planets now described, ν Oct Ab remains unprecedented in terms of the system’s geometry. It still provides many opportunities for exploring unexpected dynamical models of planet formation and orbit stability, as well as exceptional observational opportunities for such a bright, short-period system’s orbital behaviour. Recently found evidence that the secondary star may be a white dwarf was reported in the Introduction which would have a significant bearing on such studies. As more evidence accumulates only in favour of the planet, the flip-side of irrefutable evidence that the planet is instead an illusion is how unexpected any non-planetary alternative would then be.

We began by confirming how thermally-stable ν Oct A’s photosphere continues to be. This allowed us to confidently claim the photosphere, which has produced the enigmatic RVs for over a decade, is highly unlikely to contribute any variability to our chromosphere indices, nor be the source of the planet-like signal. Knowing the thermal stability of the photosphere is a useful advantage for any chromosphere study, a detail not commonly reported.

It is no doubt partly due to ν Oct A’s quiescence that has allowed our study of its Ca II spectra with such low S/N and successfully pursue our atypical methods. It is also this stability that has helped us critically examine the telluric line contribution to our $H\alpha$ spectra and quite clearly reveal its quasi-periodic behaviour and origin. All our results strongly imply they record mostly random processes and not something systematically cyclic.

Because similar studies use data that may be at least moderately correlated it seems that covariance deserves closer scrutiny in such cases. Even though the covariance terms have opposite signs, the correlation coefficients may still cause the covariance terms to increase the errors significantly – as our Ca II results demonstrate. Our methods for analysing low- S/N spectra may allow other so-far neglected archival material to be recovered usefully as we quite surprisingly achieved here. Finally, we introduced a simply described classification system for retrograde orbits that appears effective for our purposes, and may be of sufficient merit for use by others.

ACKNOWLEDGEMENTS

We appreciate the anonymous referee's several suggestions that led to helpful improvements. DJR thanks M. F. Reid, then Physics & Astronomy HoD, for renewing his Research Fellow status (2018–2020) allowing continuing access to academic and IT resources including the assistance of O. K. L. Petterson. DJR is also grateful to the UC Mt. John Observatory director K. R. Pollard and the present HoS R. Marquez for the generous allocation of observing time and research support for this project that provided us the opportunity to obtain more data for ν Oct. We thank the observing technician F. Gunn for obtaining the spectra 2018–2020 and K. R. Pollard and R. Marquez of the School of Physical and Chemical Sciences, University of Canterbury for sourcing observing and technical support for this project at the UC Mt John Observatory, including funding from The Brian Mason Trust, UC Foundation, The School of Physical and Chemical Sciences and The Otago Museum. DJR thanks M. Kürster (MPIA) and K. J. Moore (Christchurch) for helpful contributions. This research made use of LIGHTKURVE, a Python package for Kepler and TESS data analysis (Lightkurve Collaboration, 2018).

DATA AVAILABILITY

The data underlying this article will be shared on reasonable request to the corresponding author.

REFERENCES

- Arkharov A. A., Hagen-Thorn E. I., Ruban E. V., 2005, *Astron. Rep.*, 49, 526
- Barnes J. R. et al., 2020, *Nature Astronomy*, 4, 41
- Baliunas S. L. et al., 1995, *ApJ*, 438, 269
- Bergmann C. M., 2015, PhD thesis, Univ. Canterbury
- Bonavita M., Desidera S., 2020, *Galaxies*, 8, 16
- Boisse I. et al., 2009, *A&A*, 495, 959
- Campbell B., Walker G. A. H., Yang S., 1988, *ApJ*, 331, 902
- Campanella G., 2011, *MNRAS*, 418, 1028
- Catalano S., Biazzo K., Frasca A., Marilli E., 2002, *A&A*, 394, 1009
- Cincunegui C., Díaz R. F., Mauas P. J. D., 2007, *A&A*, 469, 309
- Duncan D. K. et al., 1991, *ApJSS*, 76, 383
- Dupret M.-A. et al., 2009, *A&A*, 506, 57
- Dvorak R., 1986, *A&A*, 167, 379
- Eberle J., Cuntz M., 2010, *ApJ*, 721, L168
- ESA, 1997, *The Hipparcos and Tycho Catalogues*, ESA SP-1200
- Fuhrmann K., 2004, *AN*, 325, 3
- Fuhrmann K., Chini R., 2012, *ApJS*, 203, 30
- Gaia Collaboration, 2018, *A&A*, 616, A1
- Gomes da Silva J., Santos N. C., Bonfils X., Delfosse X., Forveille T., Udry S., 2011, *A&A*, 534, A30
- Gordon I. E. et al., 2017, *J. Quant. Spectrosc. Radiat. Transf.*, 203, 3
- Gong Y.-X., Ji J., 2018, *MNRAS*, 478, 4565
- Goździewski K., Słonińska M., Migaszewski C., Rozenkiewicz A., 2013, *MNRAS*, 430, 533
- Gray D. F., Brown K., 2001, *PASP*, 113, 723
- Griffin R. F., Redman R. O., 1960, *MNRAS*, 120, 287
- Hatzes A. P., Cochran W. D., Bakker E. J., 1998, *ApJ*, 508, 380
- Hatzes A. P., Cochran W. D., Endl M., McArthur B., Paulson D. B., Walker G. A. H., Campbell B., Yang S., 2003, *ApJ*, 599, 1383
- Hatzes A. P. et al., 2015, *A&A*, 580, A31
- Hatzes A. P. et al., 2018, *AJ*, 155, 120
- Hearnshaw J. B., Barnes S. I., Kershaw G. M., Frost N., Graham G., Ritchie R., Nankivell G. R., 2002, *Exp. Astron.*, 13, 59
- Horner J. et al., 2019, *AJ*, 158, 100
- Jefferys W. H., 1974, *AJ*, 79, 710
- Kervella P., Arenou F., Mignard F., Thévenin F., 2019, *A&A*, 623, A72
- Kjeldsen H., Bedding T. R., 1995, *A&A*, 293, 87
- Kovtyukh V. V., Soubiran C., Belik S. I., Gorlova N. I., 2003, *A&A*, 411, 559
- Kratter K. M., Perets H. B., 2012, *ApJ*, 753, 91
- Kürster M. et al., 2003, *A&A*, 403, 1077
- Lightkurve Collaboration et al., 2018, *Lightkurve: Kepler and TESS time series analysis in Python*, *Astrophysics Source Code Library*, (ascl: 1218.013)
- Lin D. N. C., Bodenheimer P., Richardson D. C., 1996, *Nature*, 380, 606
- Linsky J. L., Avrett E. H., 1970, *PASP*, 82, 169
- Lisogorskyi M., Jones H. R. A., Feng F., 2019, *MNRAS*, 485, 4804
- Mayor M., Queloz D. A., 1995, *Nature*, 378, 355
- Morais M. H. M., Guipponi C. A., 2012, *MNRAS*, 424, 52
- Morton D., 2000, *ApJS*, 130, 403
- Narita N., Sato B., Hirano T., Tamura M., 2009, *PASJ*, 61, L35
- Oranje B. J., 1983, *A&A*, 124, 43
- Ortiz M. et al., 2016, *A&A*, 595, A55
- Panichi F., Goździewski K., Turchetti G., 2017, *MNRAS*, 468, 469
- Pérez Martínez M. I., Schröder K.-P., Cuntz M., 2011, *MNRAS*, 414, 418
- Press W. H., Teukolsky S. A., Vetterling W. T., Flannery B. P., 1994, *Numerical Recipes in C: The Art of Scientific Computing*, Cambridge Uni. Press, New York
- Quarles B., Cuntz M., Musielak Z. E., 2012, *MNRAS*, 421, 2930
- Quarles B., Li G., Kostov V., Haghighipour N., 2020, *AJ*, 159, 80
- Ramm D. J., 2004, PhD thesis, Univ. Canterbury
- Ramm D. J., 2015, *MNRAS*, 449, 4428
- Ramm D. J., Pourbaix D., Hearnshaw J. B., Komonjinda S., 2009, *MNRAS*, 394, 1695
- Ramm D. J. et al., 2016, *MNRAS*, 460, 3706
- Rasio F. A., Ford E. B., 1996, *Science*, 274, 954
- Reichert K., Reffert S., Stock S., Trifonov T., Quirrenbach A., 2019, *A&A*, 625, 22
- Ricker G. R. et al., 2015, *J. Astron. Telesc. Instrum. Syst.*, 1, 1
- Robertson P. et al., 2012, *ApJ*, 749, 39
- Robertson P., Endl M., Cochran W. D., Dodson-Robinson S. E., 2013, *ApJ*, 764, 3
- Rutten R. G. M., 1984, *A&A*, 130, 353
- Saio H., Wood P. R., Takayama M., Ita Y., 2015, *MNRAS*, 452, 3863
- Skuljan J., 2004, in Kurtz D. W., Pollard K., eds, *Proc. IAU Coll. 193, Variable Stars in the Local Group*, Astronomical Society of the Pacific, San Francisco, p. 575
- Stock K., Cai M. X., Spurzem R., Kouwenhoven M. B. N., Zwart S. P., 2020, *MNRAS*, 497, 1807
- Sturrock P. A., Scargle J. D., 2010, *ApJ*, 718, 527
- Trifonov T., Lee M. H., Reffert S., Quirrenbach A., 2018, *AJ*, 155, 257

- Tutukov A. V., Fedorova A. V., 2012, *Astron. Rep.*, 56, 305
Vanderburg A. et al., 2020, *Nature*, 585, 363
Walker G. A. H., Bohlender D. A., Walker A. R., Irwin A. W.,
Yang S. L. S., Larson A., 1992, *ApJ*, 396, L91
Warner B., 1969, *MNRAS*, 144, 333
Wiegert P. A., Holman M. J., 1997, *AJ*, 113, 1445
Wilson O. C., 1963, *ApJ*, 138, 832
Wilson O. C., 1978, *ApJ*, 226, 379
Wilson O. C., Bappu M. K. V., 1957, *ApJ.*, 125, 661
Winn J. N., Johnson J. A., Albrecht S., Howard A. W.,
Marcy G., W., Crossfield I. J., Holman M. J., 2009, *ApJ*, 703,
L99
Wolszczan A., Frail D., 1992, *Nature*, 355, 145
Young A., Furenlid I., Snowden M. S., 1981, *ApJ*, 245, 998
Zechmeister M., Kürster M., 2009, *A&A*, 496, 577
Zechmeister M. et al., 2018, *A&A*, 609, 12

This paper has been typeset from a \LaTeX file prepared by the author.